AIAA 99-2669

Computational Investigation of Fluidic Counterflow Thrust Vectoring

C.A. Hunter and K.A. Deere
NASA Langley Research Center
Hampton, Virginia

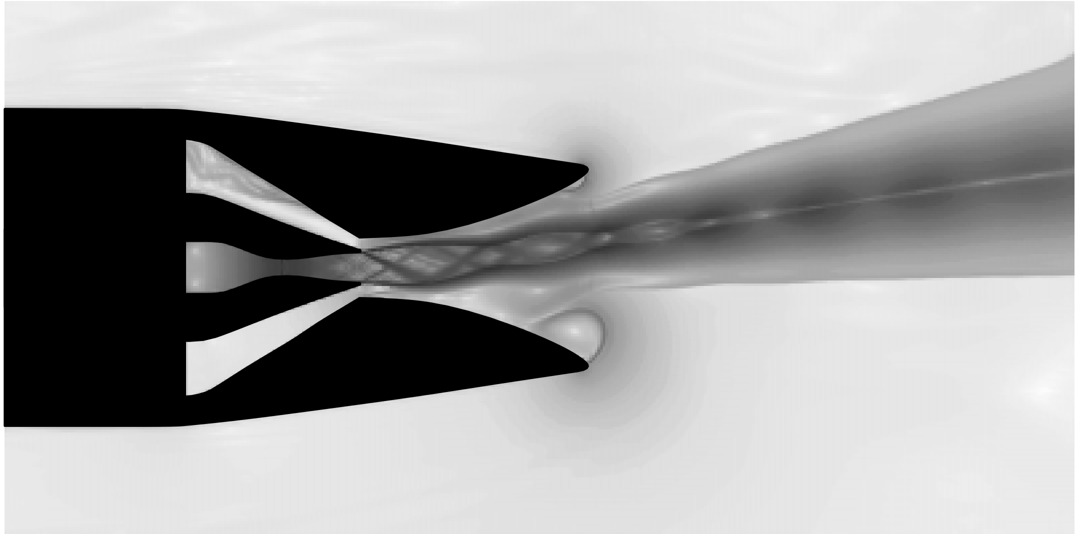

35th AIAA/ASME/SAE/ASEE
Joint Propulsion Conference & Exhibit
June 20-23, 1999 / Los Angeles, CA

AIAA-99-2669

COMPUTATIONAL INVESTIGATION OF FLUIDIC COUNTERFLOW THRUST VECTORING

Craig A. Hunter* and Karen A. Deere*
NASA Langley Research Center
Hampton, Virginia

Abstract

A computational study of fluidic counterflow thrust vectoring has been conducted. Two-dimensional numerical simulations were run using the computational fluid dynamics code PAB3D with two-equation turbulence closure and linear Reynolds stress modeling. For validation, computational results were compared to experimental data obtained at the NASA Langley Jet Exit Test Facility. In general, computational results were in good agreement with experimental performance data, indicating that efficient thrust vectoring can be obtained with low secondary flow requirements (less than 1% of the primary flow). An examination of the computational flowfield has revealed new details about the generation of a countercurrent shear layer, its relation to secondary suction, and its role in thrust vectoring. In addition to providing new information about the physics of counterflow thrust vectoring, this work appears to be the first documented attempt to simulate the counterflow thrust vectoring problem using computational fluid dynamics.

Introduction

Over the past several decades, propulsion nozzle research has led to the development of multi-mission exhaust nozzles that can provide efficient operation over a broad flight regime. In the same timeframe, however, the ability to control, mix, and suppress a supersonic jet has imposed formidable challenges, and remains one of the most critical elements of exhaust nozzle research to this day. The issue has become all the more imperative for future fighter aircraft that will rely on supersonic jet control technology for thrust vectoring, area control, and IR suppression.

Of the many exhaust nozzle technologies under consideration today, studies[1-7] have shown that thrust vectoring is perhaps the most promising, for numerous reasons. Multi-axis thrust vectoring can lead to significant tactical advantages by increasing an aircraft's agility and combat maneuverability. Thrust vectoring can provide control effectiveness superior to conventional aerodynamic surfaces at some flight conditions, and it can extend the aircraft performance envelope by allowing operation in the post-stall regime. In addition, thrust vectoring can improve takeoff and landing performance on short or damaged runways and aircraft carrier decks. Finally, the use of thrust vectoring can allow the reduction, and possibly even the elimination, of conventional aerodynamic control surfaces such as horizontal and vertical tails. This would reduce weight, drag, and radar cross section, all of which can extend an aircraft's range and capabilities. Some of the potential benefits of thrust vectoring are summarized in figure 1.

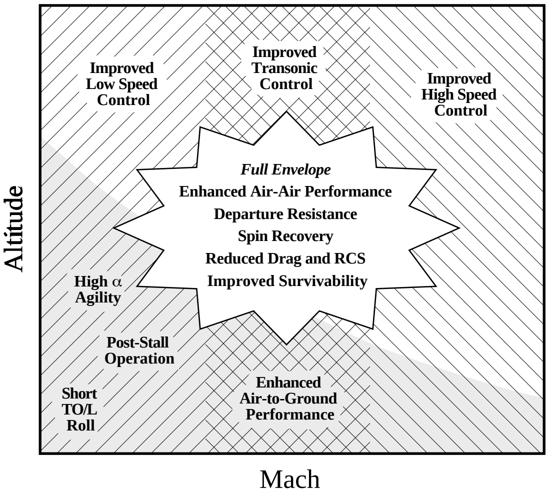

Figure 1: Potential Benefits of Thrust Vectoring

While the benefits of thrust vectoring are attractive, it's implementation can be a compromise. Current thrust-vectored aircraft such as the F-15 SMTD[8], F-18 HARV[9], X-31[10], and F-22 use mechanical systems for thrust vectoring. Though effective, these systems can be heavy and complex, difficult to integrate, expensive to maintain, and aerodynamically inefficient. Figure 2 illustrates the complexity of the vectoring system on the F-18 HARV. With the addition of stealth requirements such as IR suppression and low-observable shaping, the design and integration of an efficient mechanical thrust vectoring system becomes even more challenging.

---

* Aerospace Engineer, Configuration Aerodynamics Branch, Aerodynamics Competency. Member AIAA.

Figure 2: F-18 HARV Thrust Vectoring System

The capabilities of future aircraft will depend on the development of true multi-mission "multi-function" exhaust systems that can provide thrust vectoring and still meet other requirements. These systems need to be simple, lightweight, and inexpensive. In light of these requirements, there is a tremendous potential to improve aircraft system performance by replacing mechanical nozzle systems with efficient fixed geometry (no moving parts) configurations that use fluidic concepts for thrust vectoring and control. The current paper presents results from a computational investigation of one such concept known as counterflow thrust vectoring.

First proposed by Strykowski and Krothapali[11,12] in the early 1990's, the counterflow thrust vectoring concept is shown in figure 3. Thrust vectoring is achieved by applying suction along one periphery of a shrouded primary jet. This creates a low pressure region along the suction collar, and causes the jet to turn. As discussed by Flamm[13], this can result in effective thrust vectoring (up to 15°) with minimal suction power and low secondary mass flow requirements (less than 1% of the primary jet mass flow).

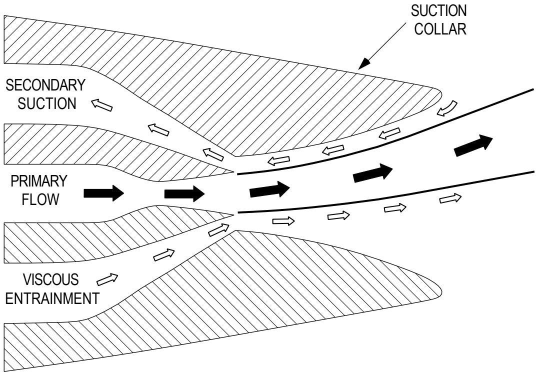

Figure 3: Counterflow Thrust Vectoring Concept

In early work[11,14,15], vectoring achieved with the counterflow concept was attributed to the generation of a "countercurrent" shear layer along the suction side of the jet. As shown in figure 4, the countercurrent shear layer has a fundamentally different character than a traditional "coflowing" shear layer. At sufficiently high velocity ratios U_2/U_1 (in excess of –0.14), the countercurrent shear layer transitions from convective instability to absolute instability, and there is a marked increase in the level of organized vortical and turbulent activity in the shear layer as it becomes globally self-excited. This results in enhanced mixing, even at high convective Mach numbers where compressibility typically suppresses the mixing process. Consequently, a countercurrent shear layer can have a growth rate more than 50% higher than a coflowing shear layer[11].

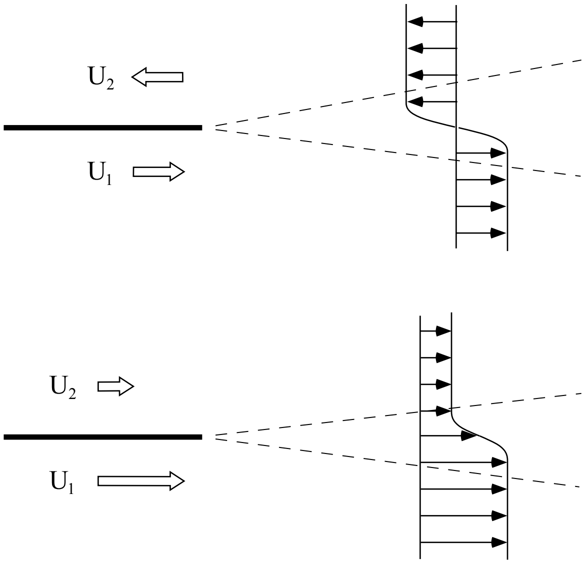

Figure 4: Countercurrent (top) and Coflowing (bottom) Shear Layers

These shear layer dynamics can be used to explain the thrust vectoring achieved with a counterflow nozzle when put in the context of a 2D jet that has one countercurrent shear layer and one coflowing shear layer (i.e., figure 3). Each shear layer entrains mass from the surrounding ambient fluid, but the presence of the suction collar inhibits this process, and causes low pressure along the collar surface. Because of the increase in organized vortical and turbulent activity in the countercurrent shear layer, it entrains more mass from the surrounding ambient fluid than the coflowing shear layer, and pressures on the counterflow side of the collar will be lower. This, in turn, creates asymmetric pressure gradients about the nozzle centerline and draws the jet off-axis. In principle, continuous control of the vector angle can be attained because the instability level of the countercurrent shear layer depends on the amount of suction applied.

Though this has been the accepted explanation for the physics of counterflow thrust vectoring, more recent work has cast some doubt on its veracity. A control volume analysis performed by Hunter and Wing[16] suggested that jet vectoring would be the same regardless of whether the secondary suction stream was counterflowing or coflowing, because both generate the same momentum flux input into the nozzle system (which is small compared to the primary jet momentum flux). According to the analysis, the suction collar pressure distribution is the important driver, independent of the direction of the secondary flow. In addition, recent experimental work by Flamm[13], which was the first to accurately measure vector angle and secondary flow rate, showed that vectoring was attained with both counterflowing and coflowing secondary streams. Finally, more recent results reported by Strykowski and Krothapalli et. al.[17] showed variations in shear layer velocity ratio in a counterflow nozzle, ranging from $U_2/U_1 = -0.10$ at the suction slot to -0.40 within the collar. This suggests that some regions of the jet may support local absolute instability, but the jet itself may not reach levels of "global" absolute instability necessary for self excitation. So, there are unresolved questions about the detailed physics of counterflow thrust vectoring.

The goal of the present study was to address some of the issues discussed above, and to make a first attempt at rigorous computational fluid dynamics (CFD) modeling of counterflow thrust vectoring. Several informal counterflow CFD studies have been attempted, unsuccessfully, but there are no known published results in this area, and the resulting experience level and knowledge base is lacking. So, this work appears to be the first documented attempt to simulate counterflow thrust vectoring using CFD.

In this study, a two-dimensional (2D) computational investigation of fluidic counterflow thrust vectoring was conducted using the Navier-Stokes code PAB3D with two-equation k–ε turbulence closure and a linear Reynolds stress model. Simulations were run at a nozzle pressure ratio (NPR) of 8, with counterflow suction slot pressures ranging from approximately 1 to 6 psi below ambient. For validation, computational results were compared to experimental data obtained by Flamm[13] at the NASA Langley Jet Exit Test Facility.

Nomenclature

F	Axial Thrust Component, lb
F_i	Ideal Isentropic Thrust, lb
H	Counterflow Nozzle Primary Jet Height, in
k	TKE per Unit Mass, ft^2/s^2
L	Counterflow Nozzle Suction Collar Length, in
M_∞	Ambient Mach Number
N	Normal Thrust Component, lb
NPR	Nozzle Pressure Ratio, $NPR = p_{oj}/p_\infty$
p	Static Pressure, psi
p_∞	Ambient Pressure, psi
p_{oj}	Jet Total Pressure, psi
p_2	Upper Secondary Slot Static Pressure, psi
p_3	Lower Secondary Slot Static Pressure, psi
$\Delta p_{3\text{-}2}$	Secondary Slot Pressure Differential, psi
Δp_{slot}	Upper Secondary Slot Gage Pressure, psi
R	Resultant Thrust, lb, $R = [F^2 + N^2]^{1/2}$
R/F_i	Resultant Thrust Efficiency Ratio
S^*	Deviatoric Mean Flow Srain Rate, 1/s
t	Time, s
T_∞	Ambient Temperature, °R
T_{oj}	Jet Stagnation Temperature, °R
TKE	Turbulent Kinetic Energy, lb/ft^2
u_i	ith Component of Mean Flow Velocity, ft/s
U_1	Primary Nozzle Exit Velocity, ft/s
U_2	Upper Secondary Slot Exit Velocity, ft/s
U_2/U_1	Shear Layer Velocity Ratio
$\langle u_i' u_j' \rangle$	Reynolds Stress Tensor, ft^2/s^2
w_p	Primary Nozzle Weight Flow Rate, lb/s
w_s	Upper Secondary Slot Weight Flow Rate, lb/s
w_s/w_p	Secondary to Primary Weight Flow Ratio
x	Streamwise Suction Collar Coordinate, in
y	Vertical Coordinate, in
y^+	Boundary Layer Law of the Wall Coordinate
x_i	ith Spatial Coordinate, ft
δ	Thrust Vector Angle, degrees, $\delta = \tan^{-1}(N/T)$
δ_i	Ideal Thrust Vector Angle, degrees
δ_{ij}	Kronecker Delta Tensor
ε	Dissipation Rate of k, ft^2/s^3
ρ_1	Primary Nozzle Exit Density, $slug/ft^3$
$\rho_1 U_1^2$	Primary Momentum Flux per Unit Area, psi
ν	Kinematic Viscosity, ft^2/s
ν_t	Turbulent "Eddy" Viscosity, ft^2/s
ψ	Secondary Suction Parameter

Computational Fluid Dynamics Simulation

The NASA Langley Reynolds-averaged Navier Stokes (RANS) computational fluid dynamics (CFD) code PAB3D was used in conjunction with two-equation k-ε turbulence closure and a linear Reynolds stress model to simulate nozzle flows in this investigation. PAB3D has been well tested and documented for the simulation of aeropropulsive and aerodynamic flows involving separation, mixing, thrust vectoring, and other complicated phenomena[18-22]. Currently, PAB3D is ported to a number of platforms and offers a combination of good performance and low memory requirements. In addition to its advanced preprocessor which can handle complex geometries through multi-block general patching, PAB3D has a runtime module capable of calculating aerodynamic performance on the fly and a postprocessor used for follow-on analysis.

Flow Solver and Governing Equations

PAB3D solves the simplified Reynolds-averaged Navier-Stokes equations in conservative form, obtained by neglecting streamwise derivatives of the viscous terms. Viscous models include coupled and uncoupled simplified Navier-Stokes and thin layer Navier-Stokes options. Roe's upwind scheme is used to evaluate the explicit part of the governing equations, and van Leer's scheme is used for the implicit part[22]. Diffusion terms are centrally differenced, inviscid terms are upwind differenced, and two finite volume flux-splitting schemes are used to construct the convective flux terms[22]. PAB3D is third-order accurate in space and first-order accurate in time. For numerical stability, various solution limiters can be used, including min-mod, van Albeda, and Spekreijse-Venkat[22]. The code can utilize either a 2-factor or 3-factor numerical scheme to solve the governing equations.

For the present study, the 2D problem was defined by j and k indices in a single i = constant plane (the j index was oriented in the streamwise flow direction). With this arrangement, explicit sweeps in the i direction were not needed, and it was possible to solve the entire problem implicitly with each iteration (using the van Leer scheme). This strategy speeds convergence and reduces computational time. Based on previous experience, the uncoupled simplified Navier-Stokes viscous option and modified Spekreijse-Venkat limiter were selected.

Turbulence Closure

In simulating turbulence, transport equations for the turbulent kinetic energy per unit mass (k) and the dissipation rate of k (ε) are uncoupled from the mean flow RANS equations and can be solved with a different time step to speed convergence. These turbulence transport equations are of the standard linear form shown below, and are solved by the same numerical schemes discussed above. The constants in the ε equation assume their standard values of $C_{\varepsilon 1}$=1.44, $C_{\varepsilon 2}$=1.92, σ_k=1, and σ_ε=1.3. In this work, the turbulent viscosity coefficient C_μ was taken to be constant and equal to 0.09.

$$\frac{Dk}{Dt} = \frac{\partial}{\partial x_j}\left[\left(\nu + \frac{\nu_t}{\sigma_k}\right)\frac{\partial k}{\partial x_j}\right] - \left\langle u_i' u_j' \right\rangle \frac{\partial u_i}{\partial x_j} - \varepsilon \qquad [1]$$

$$\frac{D\varepsilon}{Dt} = \frac{\partial}{\partial x_j}\left[\left(\nu + \frac{\nu_t}{\sigma_\varepsilon}\right)\frac{\partial \varepsilon}{\partial x_j}\right] - C_{\varepsilon 1}\frac{\varepsilon}{k}\left\langle u_i' u_j' \right\rangle \frac{\partial u_i}{\partial x_j} - C_{\varepsilon 2}\frac{\varepsilon^2}{k} \qquad [2]$$

$$\nu_t = C_\mu \frac{k^2}{\varepsilon} \qquad [3]$$

Two different types of algebraic Reynolds stress models – linear and nonlinear – were initially used in this study. While the linear model performed well in preliminary work, the nonlinear models (Shi-Zhu-Lumley[23] and Girimaji[24]) failed to produce a stable solution, and were not used in the final study. The linear stress model is shown in equation 4, and is based on simple mixing length and eddy viscosity theories dating back to the 1940's.

$$\left\langle u_i' u_j' \right\rangle = \tfrac{2}{3} k \delta_{ij} - 2C_\mu \frac{k^2}{\varepsilon} S_{ij}^* \qquad [4]$$

This model makes a simple analogy between apparent turbulent Reynolds stresses and laminar viscous stresses. It has a form that parallels the viscous stress tensor for a Newtonian fluid, in which stress is proportional to strain rate. The first term in equation 4 represents the isotropic effect of the turbulent kinetic energy, while the second "anisotropic" term models the linear effect of the deviatoric mean flow strain rate S*.

No matter which model chosen – linear or nonlinear – it is important to realize that all current RANS gradient-based Reynolds stress models may suffer a shortcoming in simulating the dynamics of a countercurrent shear layer. As shown in figure 5, both a countercurrent and coflowing shear layer can have the same velocity gradient $\partial u / \partial y$, and this gradient dominates both the mean flow strain rate and vorticity in this type of flow. From the standpoint of gradient based stress models, there will be little or no distinction between coflowing and countercurrent streams, and the calculated Reynolds stress will be virtually the same in each case. This is an important fact that must be taken into consideration when modeling a countercurrent shear layer. The modeling of separated flows suffers from the same problem, but has received little attention due to the fact that separated regions are usually small compared to the global aerodynamic scale of the problem at hand. Results from the present study should indicate whether or not this stress model limitation affects the simulation of a counterflowing jet, where the countercurrent shear layer dominates the flow.

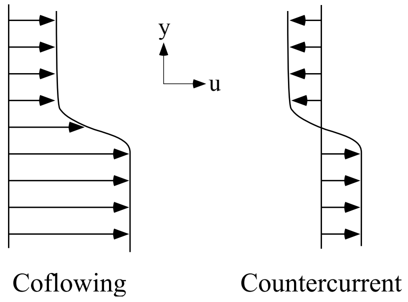

Figure 5: Shear Layers with the same Velocity Gradient

Computational Model

The 2D nozzle geometry used in this study was based on the experimental model used by Flamm[13]. Basic nozzle details are presented in figure 6. The primary convergent-divergent nozzle had an expansion ratio of 1.69, a design NPR of 7.82, and a fully expanded exit Mach number of 2.0 (the experimental model had a constant width of 4.5 inches and a nominal throat area of 3 square inches). Secondary flow ducts were located above and below the primary nozzle, each having a slot height approximately 41% of the primary nozzle exit height. The nozzle system was shrouded by a curved suction collar that terminated with a 27.8° angle at the exit nose radius.

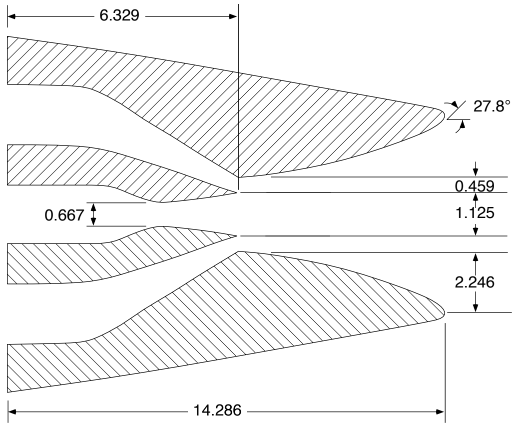

Figure 6: Counterflow Nozzle Model Details. Dimensions in inches.

A wireframe layout of the 2D multiblock finite volume grid used in the computational simulation is presented in figure 7. The grid contained 58 blocks totaling 301,392 cells (622,956 points), and was symmetric about the nozzle centerline. The ambient region surrounding the counterflow nozzle extended about 40 primary nozzle throat heights upstream and downstream of the primary nozzle exit, and 77 throat heights above and below the jet axis.

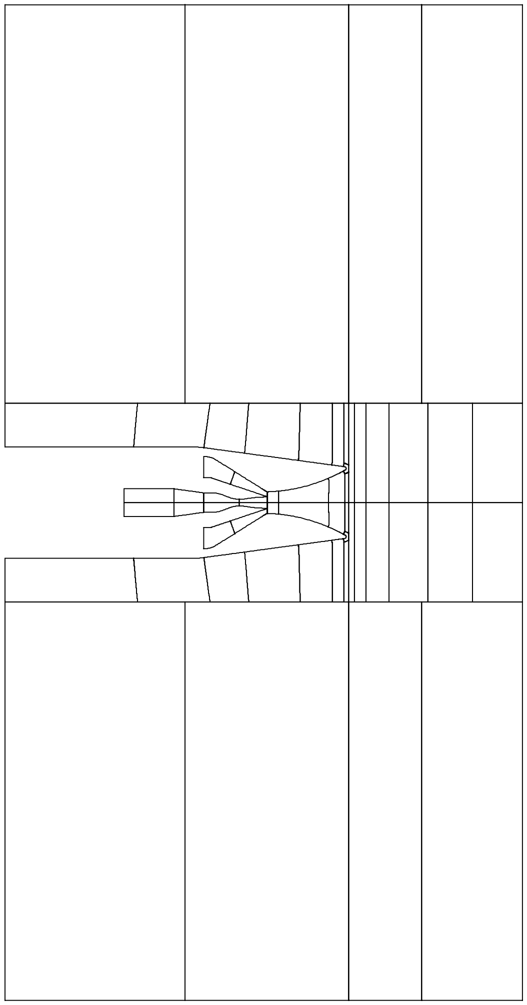

Figure 7: Computational Grid – Wireframe Sketch

A closeup view of the grid around the counterflow nozzle is shown in figure 8. The nozzle grid was characterized by boundary layer gridding with an expansion ratio of about 18% and a first cell height of approximately $y^+ = 0.5$. The collar region of the nozzle was densely gridded in an attempt to capture the complicated shear layer physics of counterflow thrust vectoring. To provide adequate simulation of vectored jet flow, the dense grid distribution extended downstream, fanning out to cover a region approximately ±30° from the centerline axis.

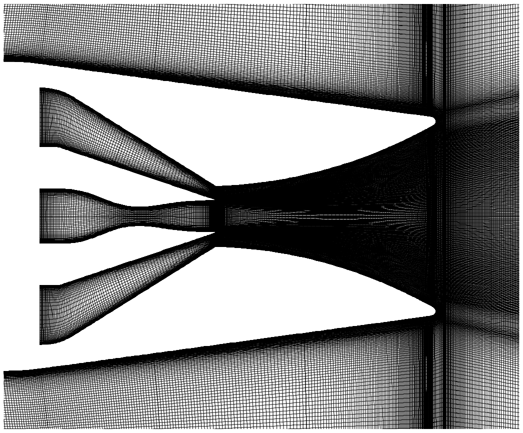

Figure 8: Counterflow Nozzle Grid

Initial and Boundary Conditions

The static ambient region surrounding the nozzle was defined by a subsonic inflow condition (T_∞=530°R, p_∞=14.7 psi, M_∞=0.07) on the upstream face, a characteristic boundary condition on the upper and lower faces, and a first order extrapolation outflow condition on the downstream face (flow is left to right). The outflow condition was chosen to limit the influence of the downstream far field boundary, which was relatively close to the nozzle exit. This approach was taken in an effort to minimize the amount of grid needed to simulate the vectored jet once it left the nozzle.

Stagnation conditions were applied to the inflow duct upstream of the primary nozzle, and were chosen to match experimental conditions for T_{oj} and p_{oj} at an NPR of 8. Counterflow suction was set by applying a similar stagnation boundary condition to the left face of the upper secondary slot, with total pressures ranging from approximately 1 to 6 psi below ambient (p_∞). The boundary condition could accommodate inflow or outflow, depending on whether the secondary stream was counterflowing or coflowing. The lower secondary slot was set to have ambient stagnation conditions. All solid walls were treated as no-slip adiabatic surfaces.

In order to initialize the turbulence transport equations and ensure the formation of a turbulent boundary layer in the counterflow nozzle, wall "trip" points were placed in the primary and secondary ducts. At these points, k was specified based on calculations involving the mean flow velocity and vorticity and a user specified turbulence intensity ratio. A corresponding value of ε was calculated based on the simplifying and reasonable assumption that the production of TKE was equal to the dissipation of TKE at the trip point. Once turbulence was established inside the nozzle, the trip points were turned off.

Solution Procedure and Postprocessing

All solutions presented in this paper were obtained by running PAB3D on an SGI Octane workstation with a 195Mhz MIPS-R10000 CPU. To speed convergence and evaluate possible grid dependence, mesh sequencing was used to evolve solutions through coarse (1/4 resolution), medium (1/2 resolution), and fine (full resolution) grids. Local timestepping was used with global CFL numbers ranging from about 0.5 to 15. Depending on the counterflow suction pressure and complexity of flow in the nozzle, it took about 14,000 iterations and 40 hours of CPU time to obtain a fully converged solution. Convergence was judged by tracking integrated performance calculations until they settled out over at least 1000 iterations.

An independent postprocessor was used to compute thrust vector angle, secondary mass flow ratio, and resultant thrust efficiency by integrating pressure, mass flux, and momentum flux over a fixed control volume. The postprocessor was also used to extract flowfield diagnostic data and construct schlieren-like images of nozzle flow[25]. These images were obtained by calculating the density gradient and combining it with a simulated optical "cutoff" effect. All images presented in this paper were generated with a root mean square average of horizontal and vertical cutoffs, and thus show sensitivity to both streamwise and transverse density gradients.

Control Volume Analysis

In previous experimental work[11-15], the upper suction slot gage pressure "Δp_{slot}" was used as the independent "input" parameter because it corresponded well with secondary suction pump settings. However, this often resulted in non-zero vector angles at Δp_{slot} = 0, due to asymmetries and peculiarities in model hardware and suction plumbing between upper and lower slots. Modeling these details (or discrepencies) would be difficult or impossible from a computational standpoint. In an effort to collapse data from numerous experiments, Hunter and Wing[16] conducted a control volume analysis of counterflow thrust vectoring, which was later adapted by Flamm[13]. The same analysis was used in the present study to develop a parameter for the presentation of data.

Based on a simplification of Hunter and Wing's analysis[16], the ideal thrust vector angle obtained with counterflow can be approximated by:

$$\delta_i = \tan^{-1}\left(\frac{p_3 - p_2}{\rho_1 U_1^2}\frac{L}{H}\right) \qquad [5]$$

where $p_3 - p_2$ is the difference in static pressure between the lower and upper slots, $\rho_1 U_1^2$ is the primary jet momentum flux per unit area, L is the suction collar length, and H is the primary jet height. See figure 9 below. Here, the numerator $(p_3 - p_2)L$ represents the "normal force" (N) generated by the upper/lower suction slot pressure difference acting over the collar length, and the denomenator $\rho_1 U_1^2 H$ represents the "axial force" (F) generated by the momentum flux of the primary jet (all forces are per unit width). So, δ_i represents the ideal thrust vector angle that would be obtained given these primary and secondary pressure and momentum flux inputs.

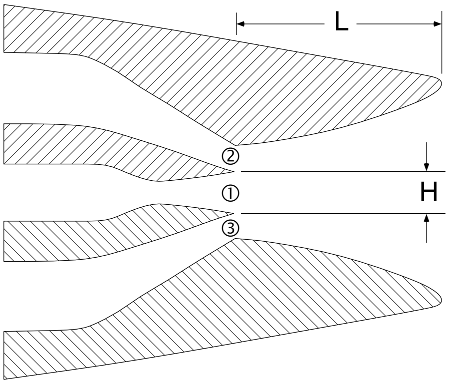

Figure 9: Control Volume Analysis Definitions

Using these results as guidance, the parameter:

$$\psi = \frac{p_3 - p_2}{\rho_1 U_1^2} \frac{L}{H} \qquad [6]$$

was selected as the independent input variable for the presentation of experimental and computational results in this investigation. Slot pressures p_3 and p_2 were obtained by a point measurement of the static pressure at each slot exit (on the suction collar) from both the experimental data and the computational solution. The primary jet momentum flux per unit area $\rho_1 U_1^2$ was estimated based on NPR from the experiment and integrated from the computational solution. Both methods agreed to within 0.5%.

Results

In the results that follow, some experimental data will show a jump, which occurred when the primary jet attached to the upper suction collar at higher vector angles, sealing off the suction slot. As discussed by Flamm[13], this phenomena is due to the Coanda effect, in which flow tends to attach itself to a nearby solid surface. Since jet attachment was hysteretic in the experiment, it essentially defined two different regimes of nozzle performance. As such, normal (no jet attachment) and attached data points will be connected by a dashed line to indicate this effect. In the experiment, jet attachment occurred at $\psi = 0.22$ for the configuration used in this study.

Jet attachment was also present in the computational simulation, but in this case, it resulted in unsteady flow and rendered the simulation highly unstable. This phenomena will be discussed in more detail later. The main effect of attachment in the computation was to define an upper limit for slot suction at $\psi = 0.43$, beyond which stable solutions could not be obtained.

Suction Slot Pressure Correlation

A correlation between the upper suction slot gage pressure Δp_{slot} and the suction parameter ψ is shown for the experiment and the computational simulation in figure 10. Both cases have the same slope, indicating good correspondence between secondary flow behavior in the experiment and the computational model. However, there is roughly a 0.5 psi offset in suction slot gage pressure between the two. As noted previously, this is due to peculiarities in the secondary flow plumbing in the experiment that were impossible to reproduce in the computational model. By using ψ as the independent variable in subsequent discussion, this difference should be immaterial. It may be important, however, when comparing these results to other work.

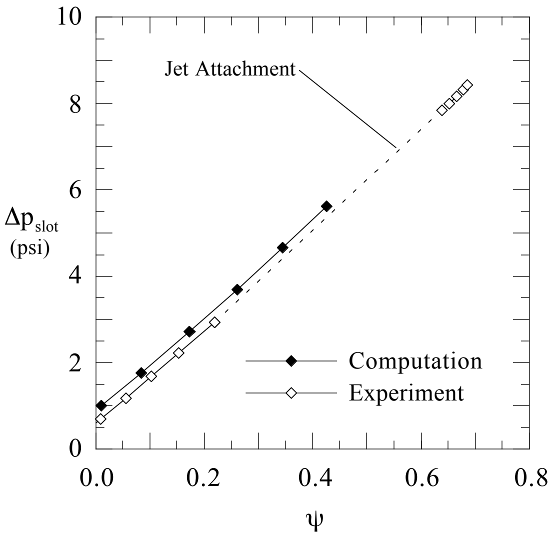

Figure 10: Suction Slot Pressure Correlation Map

Thrust Vector Angle

Thrust vectoring results for the experiment and computation are presented in figure 11, along with an "ideal" curve based on equation 5. There is excellent agreement between experiment and computation up to $\psi = 0.22$ and $\delta = 8.1°$, at which point the experimental jet jumped into the attached regime. Within this low ψ range, the data establishes a linear trend between the suction parameter and the vector angle defined by:

$$\delta = 37.34\psi \qquad [7]$$

The computational simulation continued to follow this vectoring trend out to $\psi = 0.26$ and $\delta = 9.1°$, but then departed as it too neared jet attachment at $\psi = 0.43$ and $\delta = 14.2°$.

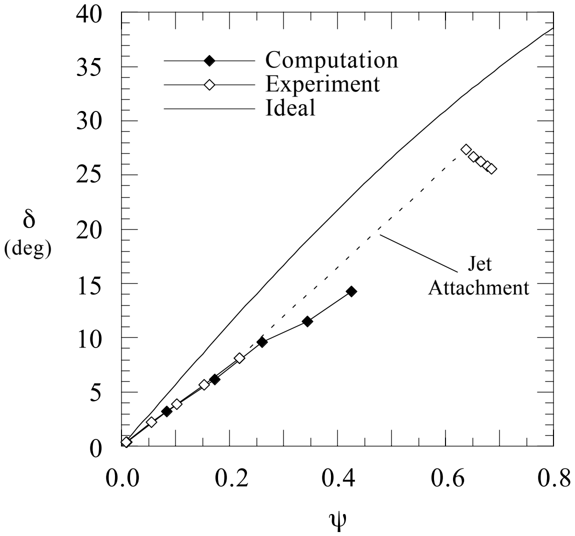

Figure 11: Thrust Vector Angle

The last five data points from the experiment show the effect of jet attachment; with only a small increase in secondary suction, ψ jumped to 0.64 and the vector angle increased to 27.4° (approximately the termination angle of the suction collar) as the jet attached to the upper collar. As discussed by Flamm[13], decreasing suction pressure beyond this point decreased δ but increased ψ, due to the fact that the supersonic primary jet had sealed off the suction slot. Recovering from this attached condition required shutting off the suction source and decreasing primary NPR in most cases, which shows the extreme hysteretic nature of this phenomena[15].

One final point of interest is the fact that the last attached experimental data point obtained, at $\psi = 0.69$ and $\delta = 25.6°$, falls along the vectoring trend defined by equation 7. This may indicate an interesting connection between the normal and attached regimes. In addition, it appears that the computational vectoring curve was "aiming" at this point when the onset of jet attachment rendered the solution unstable. This, coupled with the fact that the computational simulation jumped to attached flow at a higher value of ψ, indicates that the jet attachment process may be highly model- and geometry-dependent, unpredictable, and difficult to control. Just the current results alone demonstrate a significant difference in the attachment characteristics of a 2D computational simulation and multidimensional flow in a 2D nozzle.

Internal Performance

Thrust efficiency, which is the ratio of the resultant thrust (R) to the ideal, fully expanded "isentropic" primary nozzle thrust (F_i), is presented in figure 12. There is relatively good qualitative agreement between the two thrust efficiency curves, but the computational simulation predicted R/Fi to be about 0.5 - 0.7% higher throughout the range of ψ where the two curves overlap. This type of difference is in line with previous work involving 2D simulations[25], and is to be expected, since the 2D computational model does not account for viscous losses on the nozzle sidewalls present in the experiment. Putting this difference aside, both the experiment and the computation show a small decrease in thrust efficiency, on the order of 1.5%, as the primary jet is vectored. This indicates that counterflow thrust vectoring is relatively efficient, and will not cause a significant thrust penalty due to flow turning.

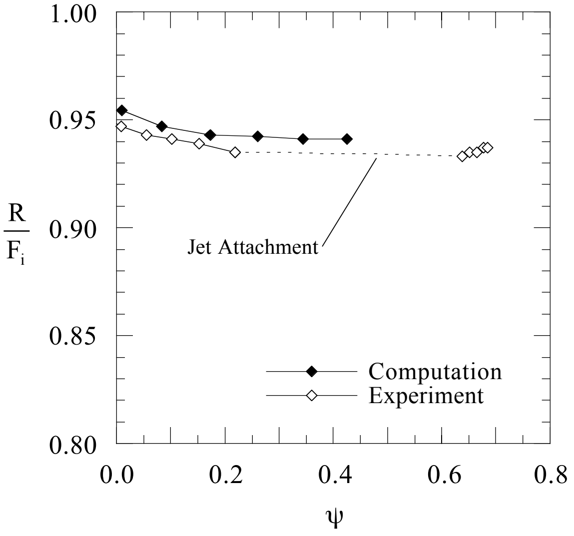

Figure 12: Thrust Efficiency Comparison

In the experiment, the primary nozzle discharge coefficient (the ratio of actual to ideal weight flow rate) was measured to be 0.9970-0.9971 over the range of ψ tested. This compares favorably with the values of 0.9953-0.9954 obtained from the computation.

Secondary Weight Flow

The ratio of secondary to primary weight flow is presented in figure 13, plotted against the suction parameter ψ. Here, positive values of w_s/w_p indicate coflow, while negative values indicate counterflow. The experiment and computation show a similar trend, with regimes of coflow and counterflow, although the two trends are shifted slightly by $\Delta\psi \approx 0.1$. Important features to note are, first, that both the experiment and computational simulation demonstrate that vectoring can be attained with coflowing and counterflowing secondary streams (this detail will be revisited and clarified below). In addition, both the experiment and the computation had very low secondary weight flow rates, approximately 0.5–1% of the primary jet flow rate, for ψ values ranging from about 0.06 to 0.43. This confirms that counterflow thrust vectoring has minimal secondary flow requirements.

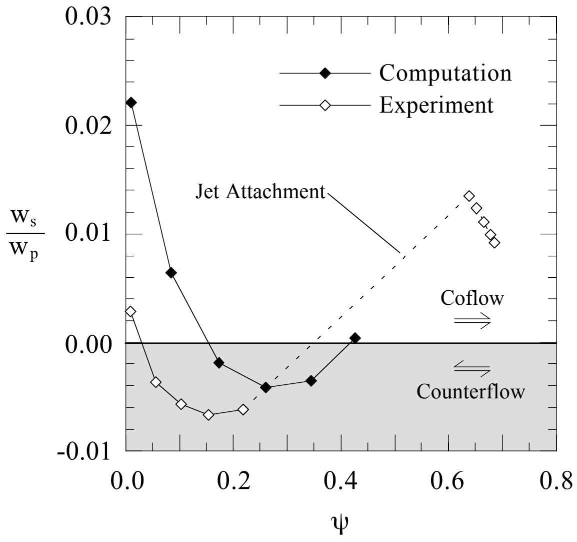

Figure 13: Secondary Weight Flow Ratio

Computational Schlieren Images

Schlieren images, obtained by postprocessing the computational solution for sensitivity to streamwise and transverse density gradients, are presented in figures 14 through 19. These images illustrate the flowfield details corresponding to the normal (no jet attachment) regime of nozzle operation for $0.01 \le \psi \le 0.43$. Overall, the computational solutions look well behaved, with good resolution of the primary jet shock structure. In all the flowfield images, separation bubbles are present on both suction collars. As the jet was vectored, the lower separation bubble grew larger and the upper separation bubble became smaller.

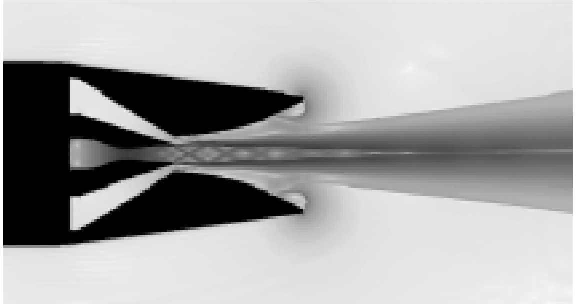

Figure 14: $\psi = 0.01$, $w_s/w_p = 0.0221$, $\delta = 0.4°$

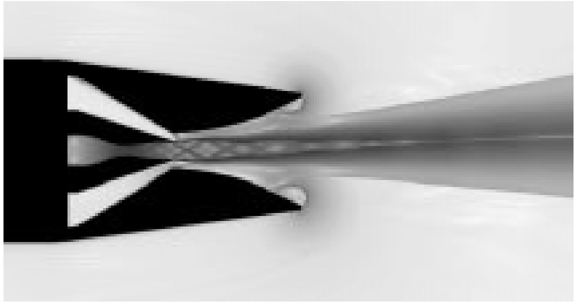

Figure 15: $\psi = 0.08$, $w_s/w_p = 0.0064$, $\delta = 3.2°$

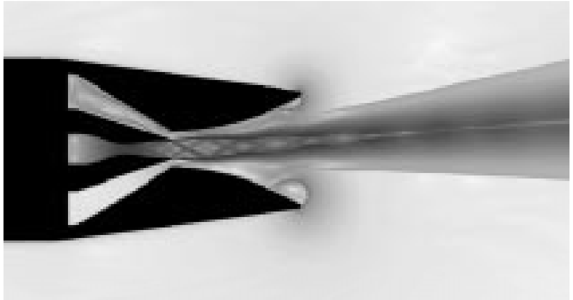

Figure 16: $\psi = 0.17$, $w_s/w_p = -0.0019$, $\delta = 6.2°$

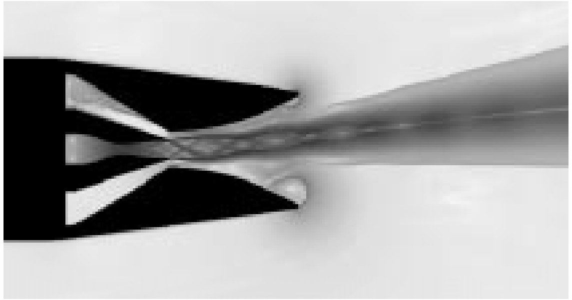

Figure 17: $\psi = 0.26$, $w_s/w_p = -0.0042$, $\delta = 9.1°$

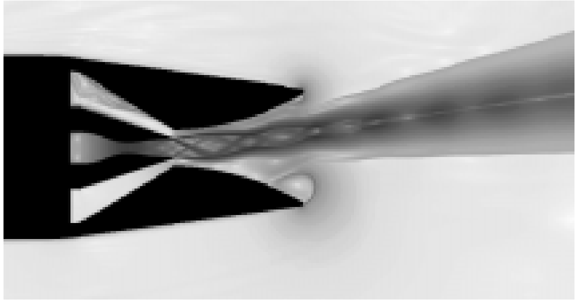

Figure 18: $\psi = 0.34$, $w_s/w_p = -0.0036$, $\delta = 11.5°$

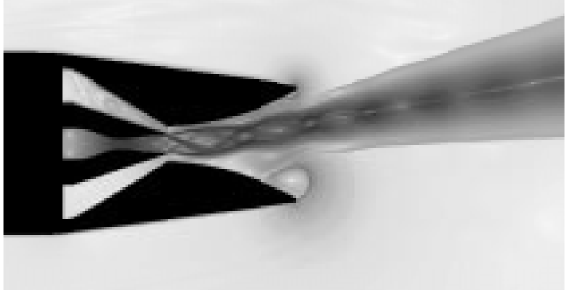

Figure 19: $\psi = 0.43$, $w_s/w_p = 0.0004$, $\delta = 14.3°$

The schlieren images also show the behavior of the secondary flow. In figures 14 and 15, the secondary stream was coflowing, and there is little activity in the upper suction slot. That changed with the onset of counterflow in figures 16, 17, and 18. In these images, there is significant flow activity in the upper secondary duct, likely due to the fact that secondary suction was entraining ambient flow through the nozzle collar. The flow activity subsided with the return back to coflow in figure 19.

Upper Suction Collar Pressures

Normalized gage pressures along the upper suction collar are presented in figure 20. Experimental centerline (open symbols) and sideline (closed symbols) data are shown for $0.06 \le \psi \le 0.22$, and computational results are given for $0.01 \le \psi \le 0.26$. Note that $x/L = 0$ at the suction slot exit and $x/L = 1$ at the end of the suction collar. Though direct comparison at a common value of ψ is not possible, there is good qualitative correspondance between the experimental centerline data and computational results, with similar features and some overlap. In particular, a comparison of experimental centerline data for $\psi = 0.10$ with computational results for $\psi = 0.08$ shows excellent agreement.

In comparing computational results with centerline experimental data, there are minor differences in the nature of the pressure distributions near the end of the suction collar, from $x/L = 0.8$ to 1.0. This is likely due to differences in separated flow behavior between the 2D simulation and 3D flow in the experimental nozzle. Comparing centerline and sideline experimental data shows that flow inside the nozzle was in fact 3D at the higher values of ψ. As discussed by Hunter[25], this sort of discrepancy between a 2D computational simulation and 3D flow inside a 2D nozzle is typical when separation occurs.

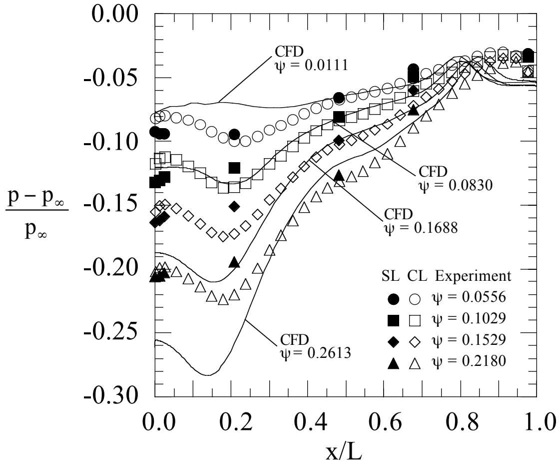

Figure 20: Top Collar Pressure Distributions

Internal Flow Details

In an effort to better understand the physics of the counterflow thrust vectoring process, the internal flowfield of the counterflow nozzle will be looked at in more detail. In the discussion that follows, two computational cases will be examined:

Case	ψ	w_s/w_p	δ
1	0.08	0.0064	3.2°
2	0.26	– 0.0042	9.1°

Note that case 1 had a coflowing secondary stream, while case 2 had a counterflowing secondary stream.

Normalized streamwise velocity contours for case 1 (coflowing) are shown in Figure 21, where u velocities are normalized by the primary jet exit velocity U_1. In the jet shear layer region, these contours effectively represent the shear layer velocity ratio U_2/U_1. Positive values of U_2/U_1 indicate forward flow, while negative values indicate reverse (countercurrent) flow. In the upper collar region, U_2/U_1 varied from 0.05 at the secondary slot exit (confirming that the secondary stream was coflowing) to a maximum negative value of –0.15 midway down the collar, and then back down to –0.10 near the collar exit. Further downstream, U_2/U_1 returned to positive values outside the nozzle. Though there was no suction in the lower slot (it was open to ambient pressure), similar behavior occurred in the separated lower collar region.

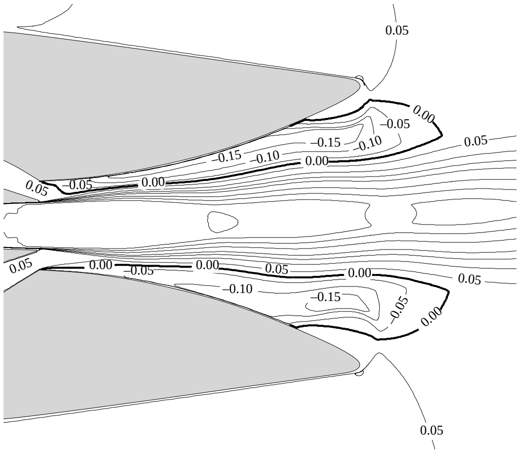

Figure 21: Normalized Velocity Contours, Case 1

Streamlines for case 1 are presented in Figure 22, and clearly show the pattern of flow in the upper collar region. External freestream flow entered the nozzle, separated around the collar nose, and then traveled upstream along the collar surface, generating a large region of reverse flow. This ended just downstream of the suction slot exit, as the external reverse flow met the forward flowing secondary stream and turned back to flow parallel with the primary jet. A stagnation region is visible about one slot height downstream of the upper slot exit, where the primary, secondary, and reverse flows met. Flow in the lower collar region exhibited similar behavior, though the lower secondary stream penetrated further out before mixing with the primary jet and separated flow on the lower collar.

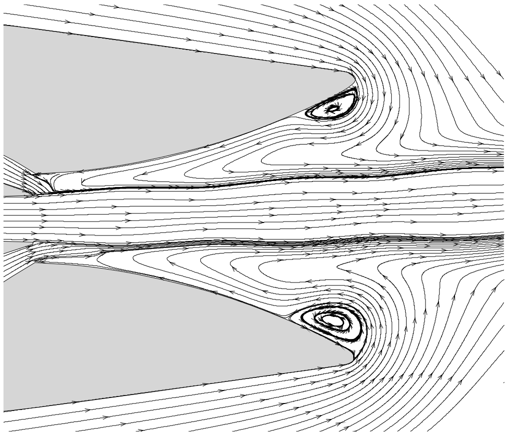

Figure 22: Streamlines, Case 1

Normalized streamwise velocity contours for case 2 (counterflowing) are shown in figure 23. These contours are similar to case 1, with a few notable differences. First, flow at the upper secondary slot exit had a negative velocity ratio of $U_2/U_1 = -0.05$, indicating that the secondary stream was indeed counterflowing. In addition, the maximum negative velocity ratio in the upper collar region was –0.25, larger than case 1. This indicates the presence of a stronger reverse flow in case 2.

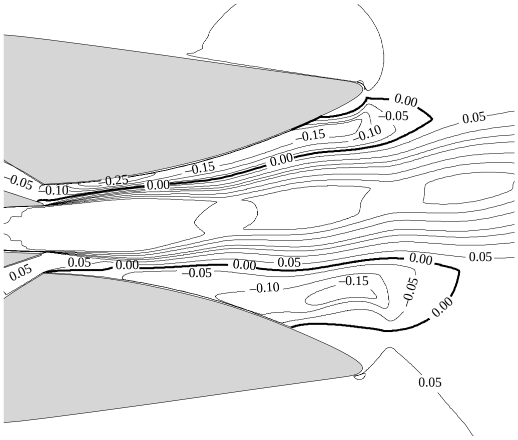

Figure 23: Normalized Velocity Contours, Case 2

Case 2 streamlines are shown in figure 24. As with velocity contours, these are similar to case 1, but there is a major difference near the upper secondary slot. Here, the external reverse flow split into two streams; one turned to coflow downstream with the primary jet, and the other continued upstream into the secondary duct. The division between these two flows can be seen just inside the secondary duct, where a stagnation point formed on the lower surface, short of the exit. This differs significantly from case 1, where three flows met outside the secondary slot.

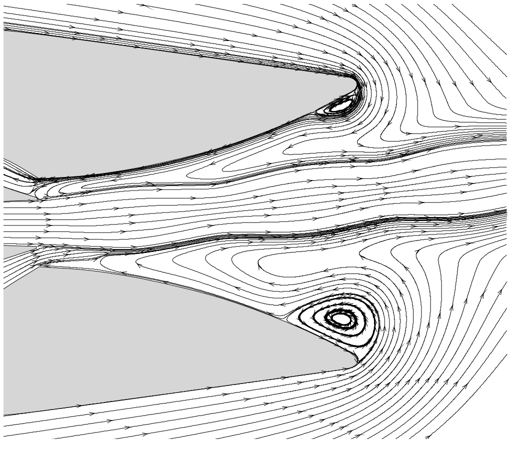

Figure 24: Streamlines, Case 2

Together, all of these observations lead to several important conclusions. First, a countercurrent shear layer was generated in both cases, though it was limited in extent and existed only within the suction collar. In the collar region, reverse velocity ratios were large enough (less than –0.14) to support local absolute instability, but the jet itself did not reach levels of global absolute instability necessary for self excitation. This agrees with results reported by Strykowski and Krothapalli et. al.[17].

In addition, though the integrated secondary weight flow for case 1 was positive (coflowing), it is clear that there was enough suction to establish a countercurrent shear layer within the suction collar, even if it was limited in extent. This may help to explain the experimental results obtained by Flamm[13], who obtained vectoring with a coflowing secondary stream, but concluded that a countercurrent shear layer was not generated. Based on computational results, it appears that the net weight flow rate of the secondary stream may be a poor indication of the state of the jet shear layer. Results from the present study indicate that a countercurrent shear layer can be generated with a coflowing or counterflowing secondary stream. As such, the distinction between a counterflowing secondary stream and a countercurrent shear layer needs to be made clear.

Finally, even though the focus has been on the upper collar region, it is interesting to note that flow in the separated lower collar region of both cases 1 and 2 is somewhat similar to the upper collar flow of case 1 (low suction coflowing secondary stream). This suggests that flow in the upper collar region may not specifically be related to the generation of a countercurrent shear layer, but in fact, may just be a result of separation and its associated reverse flow (present on the lower collar). The fact that there was a very small region of "countercurrent" flow in both cases 1 and 2 indicates that the vectoring achieved with the counterflow concept may not be related to the countercurrent shear layer at all. It may simply be a result of asymmetric separation control in a ducted nozzle, where the secondary suction merely serves to modify the separation region and provide a measure of control over thrust vector angle.

Concluding Remarks

A computational study of fluidic counterflow thrust vectoring has been conducted. Two-dimensional numerical simulations were run using the computational fluid dynamics code PAB3D with two-equation turbulence closure and linear Reynolds stress modeling. For validation, computational results were compared to experimental data obtained by Flamm[13] at the NASA Langley Jet Exit Test Facility. Specific conclusions from this work are as follows:

1. In general, computational results were in good agreement with experimentally measured vector angle, internal performance, and secondary flow rate, indicating that efficient thrust vectoring (less than 1.5% thrust efficiency penalty) can be obtained with low secondary flow requirements (less than 1% of the primary flow). In addition, internal suction collar pressures from the computational simulation showed favorable comparison to experimental pressures.

2. Though RANS gradient-based Reynolds Stress models make little or no distinction between coflowing and countercurrent shear layer velocity gradients, this limitation did not appear to be a shortcoming in the current study, at least from the standpoint of integrated performance parameters and nozzle internal pressures.

3. Differences in jet attachment behavior between the experiment and computation indicate that the jet attachment process may be highly model- and geometry-dependent, unpredictable, and difficult to control. The current results demonstrate a significant difference between the attachment characteristics of a 2D computational simulation and multidimensional flow in a 2D nozzle.

4. An examination of the computational flowfield for two cases, one with a coflowing secondary stream and one with a counterflowing secondary stream, revealed new details about the generation of a countercurrent shear layer and its relation to secondary suction. In both cases, a countercurrent shear layer was generated, though it was limited in extent and existed only within the suction collar. In the collar region, reverse velocity ratios were large enough to support local absolute instability, but the jet itself did not reach levels of global absolute instability necessary for self excitation. This agrees with results reported by Strykowski and Krothapalli et. al.[17].

5. Based on computational results, it appears that the net weight flow rate of the secondary stream may be an inaccurate indication of the state of the jet shear layer. Results from the present study indicate that a countercurrent shear layer can be generated with a coflowing or counterflowing secondary stream. As such, the distinction between a counterflowing secondary stream and a countercurrent shear layer needs to be made clear.

6. Results from this study suggest that flow in the upper collar region is not specifically related to the generation of a countercurrent shear layer, but in fact, may just be the result of separation and its associated reverse flow. Combined with the fact that there was a very small region of "countercurrent" flow observed in the computational simulation, this indicates that the vectoring achieved with the counterflow concept may not be related to the countercurrent shear layer at all. It may simply be a result of asymmetric separation control, where secondary suction merely serves to modify the separation region in the nozzle and provide a measure of control over thrust vector angle.

References

1. Bitten, R. and Selmon, J. “Operational benefits of Thrust Vector Control (TVC)”. High-Angle-of-Attack Technology, Volume I. J.R. Chambers, W.P. Gilbert, and L.T. Nguyen, eds. NASA CP-3149, Part 2, 1992.

2. Herbst, W. B. “Future Fighter Technologies”. Journal of Aircraft, vol. 17, no. 8. August 1980.

3. Herrick, P. W. “Propulsion Influences on Air Combat”. AIAA-85-1457, July 1985.

4. Nguyen, L.T.n and Gilbert, W.P. “Impact of Emerging Technologies on Future Combat Aircraft Agility”. AIAA-90-1304, May 1990.

5. Herrick, P. W. “Air Combat Payoffs of Vectoring/Reversing Exhaust Nozzles”. AIAA-88-3239, July 1988.

6. Costes, P. “Investigation of Thrust Vectoring and Post-Stall Capability in Air Combat”. AIAA-88-4160-CP, 1988.

7. Capone, F. J. “The Nonaxisymmetric Nozzle - It is for Real”. AIAA-79-1810, August 1979.

8. Bursey, R. and Dickinson, R. “Flight Test Results of the F-15 SMTD Thrust Vectoring/Thrust Reversing Exhaust Nozzle”. AIAA-90-1906, July 1990.

9. Regenie, V., Gatlin, D., Kempel, R., Matheny, N. “The F-18 High Alpha Research Vehicle: A High Angle-of-Attack Testbed Aircraft”. NASA TM-104253, 1992.

10. Knox, F., and Scellenger, H. “X-31 Flight Test Update”. AIAA-92-1035, February 1992.

11. Strykowski, P. J., and Krothapalli, A. “The Countercurrent Mixing Layer: Strategies for Shear-Layer Control”. AIAA 93-3260, July 1993.

12. Strykowski, P. J., Krothapalli, A., and Wishart, D. “Enhancement of Mixing in High-Speed Heated Jets Using a Counterflow Nozzle,” AIAA Journal Volume 31, number 11. November 1993.

13. Flamm, J.D. “Experimental Study of a Nozzle Using Fluidic Counterflow Thrust Vectoring”. AIAA 98-3255, July 1998.

14. Van Der Veer, Michael R. “Counterflow Thrust Vectoring of a Subsonic Rectangular Jet”. M. S. Thesis, University of Minnesota, 1995.

15. Schmid, Geoffrey F. “Design and Optimization of a Counterflow Thrust Vectoring System”. M. S. Thesis, University of Minnesota, 1996.

16. Hunter, C. and Wing, D. “Counterflow Thrust Vectoring: Control Volume Similarity Analysis”. NASA Langley Research Center White Paper, August 1995.

17. Strykowski, P. J., Krothapalli, A., and Forliti, D. J. “Counterflow Thrust Vectoring of Supersonic Jets”. AIAA 96-0115, January 1996.

18. Pao, S.P., and Abdol-Hamid, K.S. “Numerical Simulation of Jet Aerodynamics Using a Three Dimensional Navier Stokes Method (PAB3D)”. NASA TP-3596, September 1996.

19. Abdol-Hamid, K.S. “Implementation of Algebraic Stress Models in a General 3-D Navier-Stokes Method (PAB3D)”. NASA CR-4702, December 1995.

21. Abdol-Hamid, K.S., Lakshmanan, B., and Carlson, J.R. “Application of the Navier-Stokes Code PAB3D with k-ε Turbulence Models to attached and Separated Flows”. NASA TP-3480, January 1995.

22. Carlson, J.R. “High Reynolds Number Analysis of Flat Plate and Separated Afterbody Flow Using Non-Linear Turbulence Models”. AIAA 96-2544, July 1996.

23. Shih, T.H., Zhu, J., and Lumley, J.L. “A New Reynolds Stress Algebraic Equation Model”. NASA TM-106644, August 1994.

24. Girimaji, S.S. “Fully-Explicit and Self-Consistent Algebraic Reynolds Stress Model”. ICASE 95-82, December 1995.

25. Hunter, C.A. “Experimental, Theoretical, and Computational Investigation of Separated Nozzle Flows”. AIAA 98-3107, July 1998.